# REPORT DOCUMENTATION PAGE

Form Approved OMB No. 0704-0188



| 1. REPORT DATE *(DD-MM-YYYY)* | 2. REPORT TYPE | 3. DATES COVERED *(From – To)* |
|---|---|---|
| 07-05-2010 | Final Report | 1 July 2006 – 01 July 2009 |

**4. TITLE AND SUBTITLE**

Self-Excited Roll Oscillations of Non-Slender Wings

**5a. CONTRACT NUMBER**

FA8655-06-1-3058

**5b. GRANT NUMBER**

Grant 06-3058

**5c. PROGRAM ELEMENT NUMBER**

61102F

**6. AUTHOR(S)**

Professor Ismet Gursul

**5d. PROJECT NUMBER**

**5d. TASK NUMBER**

**5e. WORK UNIT NUMBER**

**7. PERFORMING ORGANIZATION NAME(S) AND ADDRESS(ES)**

University of Bath
Department of Mechanical Engineering
Bath BA2 7AY
United Kingdom

**8. PERFORMING ORGANIZATION REPORT NUMBER**

N/A

**9. SPONSORING/MONITORING AGENCY NAME(S) AND ADDRESS(ES)**

EOARD
Unit 4515 BOX 14
APO AE 09421

**10. SPONSOR/MONITOR'S ACRONYM(S)**

**11. SPONSOR/MONITOR'S REPORT NUMBER(S)**

Grant 06-3058

**12. DISTRIBUTION/AVAILABILITY STATEMENT**

Approved for public release; distribution is unlimited.

**13. SUPPLEMENTARY NOTES**

**14. ABSTRACT**

The main objective of this research is to understand the free-to-roll aerodynamics and selfexcited roll oscillations of low aspect ratio wings. Generic thin, flat-plate wing planforms for unmanned air vehicles and micro air vehicles were considered. Slender and nonslender delta wings with sweep angles between 40° and 70°, cropped delta wings, rectangular wings with aspect ratios of AR = 2 and 4, Zimmerman, and elliptical wings were investigated. Measurements of roll history, flow visualization, and PIV measurements were conducted in the free-to-roll experiments in a wind tunnel. Nonzero trim roll angles and self-induced roll oscillations were observed for most of the wings. Leading-edge vortices, tip vortices and separation bubbles play an important role in the free-to-roll aerodynamics. Hysteresis and time lag effects are behind the observed roll oscillations. The results may be useful in improving the maneuverability and gust response of unmanned air vehicles.

**15. SUBJECT TERMS**

EOARD, Aerodyanamics, Aircraft Structures, Aeroelasticity

| 16. SECURITY CLASSIFICATION OF: | | | 17. LIMITATION OF ABSTRACT | 18, NUMBER OF PAGES | 19a. NAME OF RESPONSIBLE PERSON |
|---|---|---|---|---|---|
| a. REPORT | b. ABSTRACT | c. THIS PAGE | | | Brad Thompson |
| UNCLAS | UNCLAS | UNCLAS | SAR | 38 | 19b. TELEPHONE NUMBER *(Include area code)* +44 (0)1895 616163 |

# SELF-EXCITED ROLL OSCILLATIONS OF NON-SLENDER WINGS

**Contract No: FA8655-06-1-3058**

**FINAL REPORT**

**submitted to**

**Dr. Surya Surampudi**

**European Office of Aerospace Research & Development (EOARD)**
**86 Blenheim Crescent**
**Ruislip, Middlesex HA4 7HB**
**United Kingdom**

**by**

**Professor Ismet Gursul**
**Department of Mechanical Engineering**
**University of Bath**
**Bath, BA2 7AY**
**United Kingdom**

**March 2010**

**SUMMARY**

The main objective of this research is to understand the free-to-roll aerodynamics and self-excited roll oscillations of low aspect ratio wings. Generic thin, flat-plate wing planforms for unmanned air vehicles and micro air vehicles were considered. Slender and nonslender delta wings with sweep angles between 40° and 70°, cropped delta wings, rectangular wings with aspect ratios of AR = 2 and 4, Zimmerman, and elliptical wings were investigated. Measurements of roll history, flow visualization, and PIV measurements were conducted in the free-to-roll experiments in a wind tunnel. Nonzero trim roll angles and self-induced roll oscillations were observed for most of the wings. Leading-edge vortices, tip vortices and separation bubbles play an important role in the free-to-roll aerodynamics. Hysteresis and time lag effects are behind the observed roll oscillations. The results may be useful in improving the maneuverability and gust response of unmanned air vehicles.

## 1. INTRODUCTION

Interest in small unmanned air vehicles (UAVs) and micro air vehicles (MAVs) has increased in recent years. A review of the aerodynamics of small vehicles flying at low speeds is given by Mueller and DeLaurier (2003). For fixed-wing aircraft, the effects of transition, separation bubble, and aspect ratio have been discussed in detail. The aerodynamics of low aspect ratio wings (aspect ratio, AR, below 2.0) are dominated by strong tip vortices (Pelletier and Mueller 2000; Torres and Mueller 2004).

The majority of studies on the aerodynamics of free-to-roll low aspect ratio wings are limited to slender delta wings and rectangular wings with AR below 0.5. Self-induced roll oscillations of

*slender* delta wings, referred to as "wing-rock", is a well known fluid-structure interaction, and is driven by the leading-edge vortices (Arena and Nelson 1994; Katz 1999). Previous studies showed that slender delta wing rock is possible for sweep angles larger than 75° (aspect ratio AR = 0.54). Similarly, very low aspect ratio rectangular wings exhibit wing rock for AR < 0.5, thought to be due to the proximity of the tip (or side-edge) vortices (Levin and Katz 1992; Williams and Nelson 1997). Previous experimental evidence has suggested that these limit-cycle roll oscillations are unique to *slender* delta wings and rectangular wings for which the vortices are relatively close to each other and generate a significant portion of the lift.

For smaller sweep angles, this type of wing-rock oscillations is not observed. However, the existence of equilibrium positions at nonzero roll angles was reported for a delta wing configuration with 65 degree sweep angle (Jenkins et al. 1996). The measured static rolling moment becomes zero at these nonzero trim angles in the free-to-roll experiments. It is believed that asymmetric vortex breakdown is behind this behavior. Limited amount of recent work on free-to-roll non-slender delta wings ($\Lambda \leq 60°$) (Matsuno and Nakamura 2000; Gursul et al. 2005) showed that self-induced roll oscillations are also possible, but about a non-zero mean roll angle when the wing is set near the stall angle.

Hence, apart from studies on delta wings and very low aspect ratio (AR below 0.5) rectangular wings, there have been no studies of free-to-roll aerodynamics of other planforms. In this paper, we study the free-to-roll aerodynamics of various low aspect ratio wings, which are more realistic for UAV and MAV applications. We found variety of roll behaviour, depending on the wing planform shape, which includes nonzero trim angles, self-induced roll oscillations over a

wide range of incidences, and even auto-rotation. Particle Image Velocimetry (PIV) measurements revealed the role of the separated flows in the free-to-roll behaviour of the low aspect ratio wings. The study of the free-to-roll dynamics is a first step towards better understanding of the gust response of these vehicles. Roll oscillations naturally limit the flight envelope. Understanding the effect of planform shape on the onset of the roll instabilities is therefore important.

## 2. EXPERIMENTAL METHODS

### A. Closed-loop Wind Tunnel

The high speed section of the closed-return wind tunnel at the University of Bath was used for all the testing. The test section of the wind tunnel has dimensions of 2.1 x 1.5 m, can operate at speeds of up to 50 $ms^{-1}$. The experiments in this study were conducted at tunnel speeds of up to 30 $ms^{-1}$. Figure 1 shows the working section layout, including the high-alpha rig, which allows the angle of attack to be varied as the wind tunnel is running with an accuracy of ±0.25 degrees.

### B. Free-to-Roll Device

The free-to-roll device consists of a shaft that is supported in greased bearings, so is free to rotate with minimal friction. One end of the shaft is attached to a potentiometer which outputs a varying voltage, linearly dependent on the roll angle, while the other end of the shaft attaches to the sting upon which the wing is supported. The output from the potentiometer was fed to the computer via an A-D converter at a rate of 250 Hz for 90 s over a range of angles of attack with an estimated uncertainty of $\pm 1^{o}$. From these data, the amplitude of the roll angle of the oscillations was calculated, as well as the maximum and minimum roll angles achieved during

the allotted time period. The Strouhal number of the oscillations at various angles of attack was obtained using a Fast Fourier Transform. The stings used for all the models on the free-to-roll device were in line with the roll axis of the wings themselves so there was no coning motion, just pure roll. Further details are given by Gresham et al. (2010a).

**C. Models**

Generic thin flat-plate wings studied include: slender and nonslender delta wings with sweep angles between 40° and 70°, cropped delta wings, rectangular wings with aspect ratios of AR = 2 and 4, Zimmerman, and elliptical wings. The sting used for all the wings was attached to the pressure surface of the model, resulting in a flat suction surface with no protrusions. The main dimensions of the wings are given by Gresham et al. (2009b, 2010a). All wings were thin (thickness-to-chord ration of 0.65% to 2.13%), except a thick delta wing (10%) for which the initial observations made. Both sharp leading-edges (with double bevel) and round edges (semi-circular) were used in the experiments. The models were painted matt black in order to reduce reflections created from the laser during the PIV tests. The Reynolds numbers (based on wing root chord length) are similar to flight conditions for unmanned air vehicles operating at low/transitional Reynolds numbers and are in the range 114,000 to 927,000. The moment of inertia about the roll axis for each wing was calculated using a CAD software, which had been calibrated using the measured masses of the wings, and includes the moment of inertia of the sting used.

**D. Particle Image Velocimetry (PIV) System**

A Particle Image Velocimetry (PIV) system with dual 120 mJ Nd:YAG lasers was used to capture the cross-flow velocity field in most of the experiments. In addition, near-surface velocity measurements were performed with the laser illuminating a plane parallel and close to the wing surface (1 mm from the surface). We mounted the laser on a precise traverse and initially aligned the laser parallel to and touching the wing surface. We then moved the laser sheet 1 mm away from the wing surface using the traverse. However, due to the thickness of the laser beam, we estimate an uncertainty of 0.2 mm in locating the measurement plane. We believe the topology is not sensitive to a slight misalignment. Such PIV measurements were previously used to give an indication of the near-surface topology on low sweep delta wings (Yavuz et al. 2004; Taylor and Gursul 2004). Seeding was provided by a smoke machine placed in the low-speed section of the wind tunnel. The set-up is shown in Figure 1, with the laser in this instance illuminating a cross-flow plane. Images were captured using an 8-bit TSI PowerView 4M digital camera with a resolution of 2048 x 2048 pixels and a maximum capture rate of 7.5 frames per second, producing 3.75 frames in cross correlation. An interrogation window size of 32 x 32 pixels was used to produce velocity vectors for further processing. For both the stationary wing and rolling wing cases, we used 1000 images in PIV measurements and a FFT correlation algorithm was used to obtain the velocity vectors. The measurement uncertainty for the velocity is estimated as 2% of the free stream velocity. Separate tests in the measurement planes were needed to cover the measurement domain (extent of the wing span) and only every third vector is shown in the PIV results for clarity. The results shown incorporate both dynamic cases, where the laser was triggered at specific roll angles during the roll oscillations, and stationary cases, with the wing clamped at the desired roll angle. In order to measure the strength of the side-edge

vortices from the PIV data, circulation was calculated using a line integral around the region of interest and normalized using the free stream velocity and chord length.

## 3. RESULTS

### 3.1. Flow field over a nonslender delta wing

As the aerodynamics of low aspect ratio wings are of interest in this project, we started with investigations of flow fields of nonslender delta wings. While the flow fields of slender delta wings are well known, there is relatively small focus on the nonslender wings. In a combined experimental and computational effort, we looked at the flow field of a nonslender delta wing with sweep angle of 50 degrees. We (in Bath) provided the PIV data for validation of the simulations performed by Dr. Raymond Gordnier and Dr. Miguel Visbal of the AFRL. The details of the numerical scheme are given by Gordnier et al. (2009). An example of the comparison between the experiments and simulations, for both mean and instantaneous flow, is shown in Figure 2. The effect of Reynolds number was investigated in the range of $2x10^5$ to $2x10^6$. The results are examined to provide a description of the mean and instantaneous flow structure over the delta wing, including the separated vortical flow, vortex breakdown, surface flow features, and surface boundary-layer transition near the symmetry plane. In crossflow planes normal to the vortex core, a weakening of the secondary flow and an outboard movement of the secondary separation point were observed with increasing Reynolds number both upstream and downstream of breakdown. Downstream of breakdown the vortex takes a more oval shape and is comprised of a number of small scale features that become more numerous and distinct with increasing Reynolds number. The mean flow exhibits helical substructures that corotate with the primary vortex in the shear layer that separates from the leading edge and rolls up to

form the primary vortex. These substructures decrease in wavelength and develop progressively further upstream with increasing Reynolds number. These results highlight the importance of high-order accuracy as well as the ability of the ILES approach in correctly simulating these types of transitional flows for moderate Reynolds number flows.

### 3.2. Free-to-roll dynamics of nonslender delta wings

Unusual self-excited roll oscillations for a nonslender delta wing ($\Lambda$ = 45°) with rounded leading-edge reported previously (Matsuno and Nakamura, 2000) were the main motivation behind this project. As we studied the flow features in detail for a nonslender delta wing with $\Lambda$ = 50°, detailed free-to-roll experiments were conducted using the setup shown in Figure 1. It was shown that the wing may have multiple trim positions at zero or nonzero roll angles (see Figure 3), depending on the angle of attack and the initial roll angle. The data shown in Figure 3 are for a thick wing (10%) with semi-circular leading-edge shape. It is seen that, for $\alpha$ = 15°, the trim roll angle is nonzero. For some incidences, different trim roll angles are possible depending on the initial roll angle, indicating the existence of multiple "attractors" (Jenkins et al. 1996). The mirror image of the trim roll angle (i.e, roll angle of –25° instead of +25° in Figure 3) is also possible depending on the initial roll angle at which the wing is released to roll.

For a post-stall incidence of $\alpha$ = 35°, the trim angle is consistently zero roll angle regardless of the initial roll angle as shown by the example in Figure 3. Just before the stall, self-excited roll oscillations whose mean roll angle is nonzero are possible in a narrow range of angles of attack as shown in Figure 4. The nature of these roll oscillations for this thick wing ($\Lambda$ = 50°) with rounded leading-edges appeared to be similar to the earlier findings for a nonslender delta wing

($\Lambda = 45°$) with rounded leading-edge by Matsuno and Nakamura (2000). It was speculated by Ericsson (2001) that round leading-edges are necessary for the self-excited roll oscillations for nonslender delta wings. As discussed below, we found that this is not essential.

### 3.3. Effect of leading-edge shape and thickness

One of the most important findings of this research is that round leading-edge is not necessary and roll oscillations can develop for sharp leading-edges as well, as shown in Figure 4. The amplitude of the oscillations is smaller compared to that of the wing with round leading-edge. Detailed phase-averaged PIV measurements (see Figure 5) suggest that, if the leading-edge is rounded (hence, the separation line is not fixed), unsteady separation at the leading-edge might also contribute to the roll oscillations. We systematically studied the effect of wing thickness and leading-edge shape. The thick wings with rounded edges exhibit larger roll oscillations. Nevertheless, when the separation is fixed at the leading-edge, these roll oscillations are still possible, depending on the wing sweep angle. In the rest of the investigation, we studied delta wings with sharp leading-edges and varied the sweep angle.

### 3.4. Effect of wing sweep angle

For wings with sharp leading-edges, a clear trend in the behaviour of the slender and nonslender wings emerged. This is shown for nonslender wings with $\Lambda = 40°, 45°, 50°, 52.5°, 55°$ in Figure 6 and for slender wings with $\Lambda = 57.5°, 60°, 65°, 70°$ in Figure 7. The existence of equilibrium at nonzero roll angles is common for nonslender wings, which is the result of asymmetric reattachment of the separated flows. For the nonslender wings, the nonzero roll angles are observed until the wing stalls after which the trim angle becomes zero. The stall of the free-to-

roll wing is very sudden. For slender wings, roll asymmetries decrease and the stall becomes more gradual with increasing sweep angle. For the most slender delta wing studied ($\Lambda = 70°$), the mean roll angle is virtually zero.

The self-induced roll oscillations are illustrated by the standard deviation of the roll angle shown as error bars for each wing in Figures 6 and 7. It is seen that for very low sweep angles (such as $\Lambda = 40°$ and 45°), there are no roll oscillations. With increasing sweep angle, roll oscillations first increase in magnitude and then decrease. Typically, self-induced roll oscillations are observed just before the stall for nonslender wings. For some wings, there are two different regions over which the roll oscillations are observed, the second one being during the gradual stall. As a summary, variation of the mean roll angle at angle of attack with highest standard deviation as well as variation of the maximum standard deviation as a function of sweep angle is shown in Figure 8. It is seen that the largest oscillations are observed for $\Lambda = 57.5°$. In order to understand how the roll oscillations are initiated and sustained, vortex topology in a cross-flow plane was studied.

### 3.5. Vortex topology

As a first step, we measured the cross-flow velocity for the static (clamped) wing at different angles of attack before the stall for the $\Lambda = 55°$ wing (see Figure 9). The idea was to explore the mean flow fields at the incidences before the roll oscillations appear, during the roll oscillations, and after the roll oscillations. It is seen in Figure 9 that, just before the oscillations begin, the shear layers and reattachment lines become closer to each other. Hence, we conclude that the increasing proximity of the shear layers may be triggering these oscillations. In part (iv), which

was just before the wing snapped to zero mean roll angle, the shear layers appear to merge. This becomes the precursor of the sudden stall.

Phase-averaged PIV measurements were conducted for the $\Lambda = 55°$ wing at the angle of attack with maximum roll oscillations (see Figure 10) in order to gain an understanding of the flow structure. A compact vortex on one side and a more diffused vortex structure are visible throughout the roll cycle. Movement of the vortex and separated shear layer shows hysteresis and time lag effects. This is clear when the flow fields in parts (ii) and (iv), corresponding to the mean roll angles, are compared. Overall, these features are similar to those for the thick wing discussed earlier.

As mentioned earlier, if the stall is more gradual, roll oscillations in two different regions of angles of attack may be observed (see, for example, $\Lambda = 60°$ in Figure 7). For this sweep angle, we have conducted experiments in both regions. The mean flow fields of the static wing in and around the first region are shown in Figure 11. It is seen that for the incidence before the oscillations commence, the reattachment lines are separate. As the angle of attack is increased, the reattachment points in the cross-flow plane appear to be very close. Figure 12 shows the phase-averaged flow field for the oscillating wing at $\alpha = 26.5°$. Near the maximum roll angle, the reattachment points are well separated. As the roll angle decreases, the reattachment points move closer to each other. The hysteresis is visible when the flow fields at the mean roll angles (parts (ii) and (iv)) are compared. Based on these measurements, it is concluded that the roll oscillations in the first region are similar to those previously discussed.

In the second region, there are some differences. Figure 13 shows the crossflow streamline patterns in the second region for the $\Lambda = 60°$ wing. Measurements in two cross-flow planes near the maximum and minimum roll angles are presented. It is seen that there is interaction between the shear layers near the maximum roll angle, and the distance between the reattachment points is minimum. This is the opposite behaviour to that observed in the first region. Near the minimum roll angle (which is close to zero), an asymmetric flow structure is present, demonstrating that a time lag exists. Figure 13 also shows that the crossflow patterns are somewhat different in two planes, suggesting that the three-dimensional effects may exist.

### 3.6. Effect of wing slenderness ratio

In order to investigate the effect of slenderness ratio, we considered various cropped delta wings with the same initial sweep angle of $\Lambda = 55°$ as shown in Figure 14. It is seen that as the slenderness ratio (chord/span) increases, the nonzero roll angles and roll oscillations decrease. Even a small increase in the slenderness ratio makes substantial differences in the roll response. Roll asymmetries rapidly vanish with increasing slenderness. For the most slender wing, there is no roll asymmetry. To understand the effect on the flow field, we performed PIV measurements as shown in Figure 15. Cross-flow velocity and streamlines for the stationary wing at zero roll angle are shown for the cropped delta wing in two different stations. The structure and location of the vortical flow at station (a) are very similar to those obtained for the simple delta wing with the same sweep angle (not shown here). However, the measurements at station (b) (trailing-edge) suggest that the vortices move outboard and away from the surface. Further measurements for a slender simple delta wing with $\Lambda = 70°$ (not shown here, but presented by Gresham et al., 2010b)

reveal very similar flow field to that in station (b). Hence, the location of the vortices may be a precursor of the free-to-roll dynamics.

### 3.7. Other planforms

Low aspect ratio wings shown in Figure 16, which include rectangular, elliptical and Zimmerman wings, are more realistic for MAV applications. The free-to-roll aerodynamics of these wings was investigated in detail (Gresham et al., 2009a, 2009b). Nonzero trim angles at low angles of attack, self-induced roll oscillations with increasing angle of attack and even auto-rotation in some cases were observed. An example is shown in Figure 17 for the rectangular wing with AR=2 at a Reynolds number of $Re=1.14x10^5$. Up to $Re=3.42x10^5$, the results are qualitatively similar, while the autorotation starts at a smaller incidence with increasing Reynolds number.

Detailed PIV measurements near the wing surface were performed for the static wing at zero roll angle to understand the associated flow physics. These are shown in Figure 18 for $Re=1.14x10^5$. It is seen that asymmetric development of the three-dimensional separation bubble at low incidences explains the nonzero trim angles if the wing is set free to roll. The case of $\alpha = 5°$ illustrates the asymmetric bubble for the wing with round leading-edge. It was shown by Gresham et al (2009b) that this asymmetric bubble becomes wider and a lot more symmetric if the leading-edge is sharp. Hence we conclude that small manufacturing imperfections in the leading-edge geometry may have significant effect on the flow asymmetries.

As the angle of attack is increased, this asymmetry on the wing surface disappears, and the separation bubble grows. This corresponds to the mean roll angle becoming closer to zero for the free-to-roll wing. As long as the bubble is on the wing, there are no roll oscillations. Once the reattachment is lost, roll oscillations develop. Figure 19 shows the near-surface velocity and streamlines at the mean roll angle for the static wing and for increasing and decreasing roll angle during the roll oscillations at $\alpha = 15°$. The stationary case shows a reasonably symmetrical flow structure. For the increasing roll angle and the decreasing roll angle, the flow fields are very different. It can be seen that there is no interaction between the side-edge vortices, showing that wing rock is not necessarily confined to slender wings only.

The detailed measurements (see Figure 20) show that the time lag in the strength of the vortices drives the motion. At (i) the stronger right-hand vortex drives the motion ($\Gamma/U_\infty c = -0.31$ and 0.41), while at (ii) the left-hand vortex has increased in strength ($\Gamma/U_\infty c = -0.39$) relative to the right-hand one ($\Gamma/U_\infty c = 0.18$). The left-hand vortex core is also seen to move inboard, and while one might expect this to reduce the moment arm of this vortex; this is more than compensated for by the increase in strength of the vortex. This left-hand vortex now drives the motion back through the mean roll angle (iii) at which the left-hand vortex is still stronger ($\Gamma/U_\infty c = -0.42$ and 0.36). At the minimum roll angle (iv), the right-hand vortex is much stronger ($\Gamma/U_\infty c = 0.35$) than the left-hand vortex ($\Gamma/U_\infty c = -0.22$), which provides the restoring moment for the wing. Figure 20 clearly shows the hysteresis that exists in the flow and large time lag in the development of the vortices. For example, the left-hand vortex reaches its maximum strength not at the largest roll angle, but at the mean roll angle ($\Phi$ decreasing). Hence, the phase lag is at least 90 degrees.

Figure 21 shows the variation of roll angle with angle of attack for the elliptical wing and Zimmerman wing. It is seen that these planforms also exhibit similar roll asymmetries and roll oscillations, which are believed to be associated with the tip (side-edge) vortices. The variation of the Strouhal number for all wings is shown in Figure 22. The Strouhal number is on the order of $10^{-2}$, which is in the same range as those expected for small aircraft experiencing atmospheric gusts.

## 4. CONCLUSIONS

Free-to-roll aerodynamics of low aspect ratio wings was studied. Slender and nonslender delta wings with sweep angles between 40° and 70°, cropped delta wings, rectangular wings with aspect ratios of AR = 2 and 4, Zimmerman, and elliptical wings were investigated. Measurements of roll history, flow visualization, and PIV measurements were conducted in the free-to-roll experiments in a wind tunnel.

For delta wings with low sweep angles, nonzero trim angles are typical until the wing stalls after which the trim angle becomes zero (when the flow reattachment is no longer possible). The stall angle increases with increasing sweep angle and is very sudden for nonslender wings. The stall of the free-to-roll wing becomes more gradual with increasing sweep angle. The magnitude of the roll trim angle decreases with increasing sweep angle and reaches zero at $\Lambda = 70°$. This can be attributed to the reattachment lines moving to the centerline with increasing sweep angle. In a certain range of sweep angles ($52.5^o$ to $60^o$) and just before the stall, large self-induced rolls oscillations were seen for the wings with sharp leading-edges. PIV measurements suggest that

the oscillations are initiated by the increasing proximity of the shear layers as the angle of attack is increased. Self-exited roll oscillations occur for fixed separation point at the leading-edge, but seem to be amplified when the separation is not fixed on rounded leading-edges. The maximum standard deviation of the roll oscillations found for a $57.5^o$ sweep wing. There are two different regions of angles of attack for which the wing oscillated for $\Lambda = 57.5^o$ and $60^o$.

Phase-averaged PIV measurements showed that the mechanism for the roll oscillations of the thick wing with rounded leading-edge and sweep angle of 50°, and the thin wings with sharp leading-edges and sweep angles of $55^o$ and $60^o$ is the same. A strong vortex on the left-hand wing half drives the motion near the minimum roll angle $\Phi_{min}$, while at $\Phi_{max}$ the restoring moment is created by the earlier reattachment of the right-hand shear layer (which becomes much closer to the wing surface), combined with a much smaller left-hand vortex. Hysteresis effects are significant even though typical Strouhal numbers are very low. A slightly different mechanism was revealed by the PIV measurements for the $60^o$ wing in the second region of angle of attack where the wing oscillated. These oscillations showed a different behaviour of the right-hand shear layer, although the growth and decay cycle of the left-hand vortex during the roll oscillations is similar. In this case, it is suggested that asymmetry in vortex strength caused by a time lag provides the driving motion for the roll oscillations.

For other planform shapes, non-zero trim angles at low angles of attack, self-induced roll oscillations with increasing angle of attack, and even autorotation in some cases were observed. At low incidences, near-surface velocity measurements for the stationary wing show the asymmetric development of the three-dimensional separation bubble, explaining why zero roll

angle is not stable. The separation bubble on a similar wing with sharp leading-edge is more symmetric, resulting in nearly zero trim angles. With increasing angle of attack, the separation bubble becomes more symmetric, resulting in near zero trim roll angles for the free-to-roll wing. Once the reattachment of the separated shear layer fails, the onset of large amplitude roll oscillations is observed. This angle of attack is smaller than the stall angle at which maximum lift is observed. Strouhal number of the roll oscillations is of the order of $10^{-2}$, which is in the same range as those expected for MAVs experiencing atmospheric gusts. The amplitude of the oscillations strongly depends on the planform shape. Depending on the planform, the amplitude may increase up to 90 degrees, which results in autorotation at high angles of attack.

It is also interesting to note that these self-induced roll oscillations for wings with relatively high aspect ratio (around AR = 2 to AR = 4) have not received much attention previously. Because of higher aspect ratios, no interaction between the vortex pair occurs. Cross-flow PIV velocity measurements and circulation calculations revealed that variations in the strength of the vortices drove the rolling motion. At the mean roll angle, because of the time lag in the strength of the vortices, an asymmetric flow is generated, which results in a net rolling moment in the direction of the rolling motion. Hysteresis and time-lag effects are similar to those of slender wings.

## 5. REFERENCES


Arena, A.S., and Nelson, R.C., 1994, "Experimental Investigations on Limit Cycle Wing Rock of Slender Wings," *Journal of Aircraft*, vol. 31, no. 5, pp. 1148-1155.

Ericsson, L.E., 2001, "Wing Rock of Non-slender Delta Wings," *Journal of Aircraft*, vol. 38, no. 1, pp. 36-41.

Gresham, N.T., Wang, Z., and Gursul, I., 2009a, "Self-Induced Roll Oscillations of Nonslender Wings", *AIAA Journal*, Aerospace Letter, Vol. 47, Issue: 3, March, Pages: 481-483.

Gresham, N.T., Wang, Z., and Gursul, I., 2009b, "Low Reynolds Number Aerodynamics of Free-to-Roll Low Aspect Ratio Wings", *Experiments in Fluids*, in print, online version: DOI 10.1007/s00348-009-0726-2, published online 21 August.

Gresham, N.T., Wang, Z., and Gursul, I., 2010a, "Vortex Dynamics of Free-to-Roll Slender and Nonslender Delta Wings", *Journal of Aircraft*, vol. 47, no. 1, January-February, pp. 292-302.

Gresham, N.T., Wang, Z., and Gursul, I., 2010b, "Effect of Slenderness Ratio on Free-to-Roll Wing Aerodynamics", in preparation for submission.

Gursul, I., Gordnier, R., and Visbal, M., 2005, "Unsteady Aerodynamics of Nonslender Delta Wings", *Progress in Aerospace Sciences,* vol. 41, no. 7, pp. 515-557.

Gordnier, R.E., Visbal, M.R., Gursul, I., Wang, Z., 2009, "Computational and Experimental Investigation of a Nonslender Delta Wing", *AIAA Journal,* vol. 47, no. 8, August, pp. 1811-1825.

Jenkins, J. E., Myatt, J. H., and Hanff, E. S., 1996, "Body-Axis Rolling Motion Critical States of a 65-Degree Delta Wing," *Journal of Aircraft*, Vol. 33, No. 2, pp. 268-278.

Katz, J., 1999, "Wing/vortex interactions and wing rock," *Progress in Aerospace Sciences*, Vol. 35, pp. 727-750.

Levin, D. and Katz, J., 1992, "Self-Induced Roll Oscillations of Low-Aspect-Ratio Rectangular Wings," *Journal of Aircraft,* Vol. 29, No. 4, pp. 698-702.

Matsuno, T. and Nakamura, Y., 2000, "Self-Induced Roll Oscillation of 45-degree Delta Wings," AIAA 2000-0655, 38$^{th}$ AIAA Aerospace Sciences Meeting and Exhibit, 10$^{th}$-13$^{th}$ January 2000, Reno, NV.

Mueller, T. J., and DeLaurier, J. D., 2003, "Aerodynamics of Small Vehicles", *Annual Review of Fluid Mechanics*, Vol. 35, January, pp. 89–111.

Pelletier, A. and Mueller, T.J., 2000, "Low Reynolds Number Aerodynamics of Low-Aspect-Ratio Thin/Flat/Cambered-Plate Wings," *Journal of Aircraft,* vol. 37, No. 5, pp. 825-832.

Taylor, G. and Gursul, I., 2004, "Buffeting Flows over a Low Sweep Delta Wing", *AIAA Journal,* vol. 42, no. 9, pp. 1737-1745.

Torres, G.E. and Mueller, T.J., 2004, "Low-Aspect-Ratio Wing Aerodynamics at Low Reynolds Numbers," *AIAA Journal,* vol. 42, No. 5, pp. 865-873.

Williams, D.L. and Nelson, R.C., 1997, "Fluid-Dynamic Mechanisms Leading to the Self-Induced Oscillations of LARR Wings," AIAA 97-0830*, 35$^{th}$ Aerospace Sciences Meeting & Exhibit*, January, Reno, NV.

Yavuz, M.M., Elkhoury, M., Rockwell, D., 2004, "Near-surface topology and flow structure on a delta wing", *AIAA Journal*, vol. 42, no. 2, pp. 332–340.

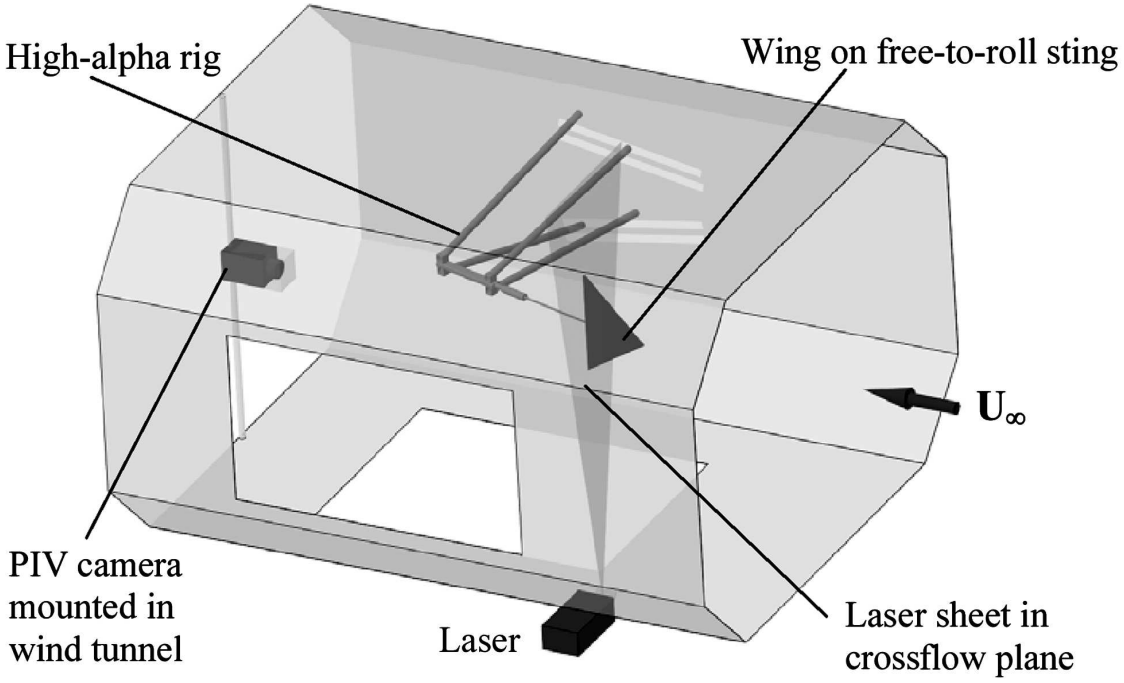


Figure 1: Schematic of the wind tunnel and experimental setup.

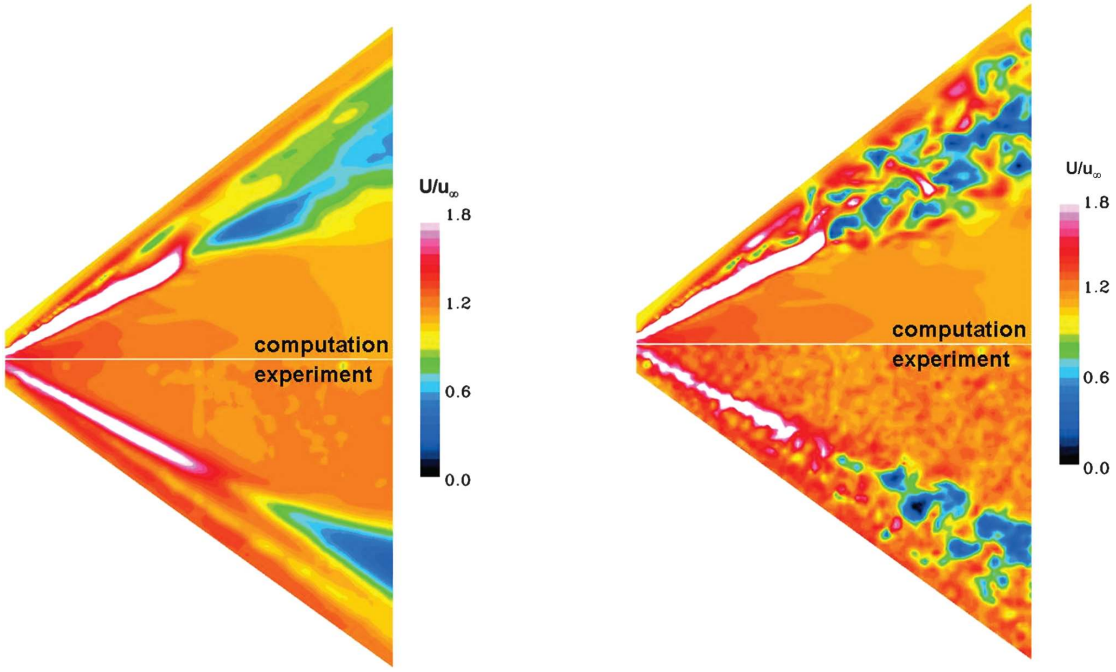


Figure 2: Comparison of mean and instantaneous flow structure between the experiments and simulations.

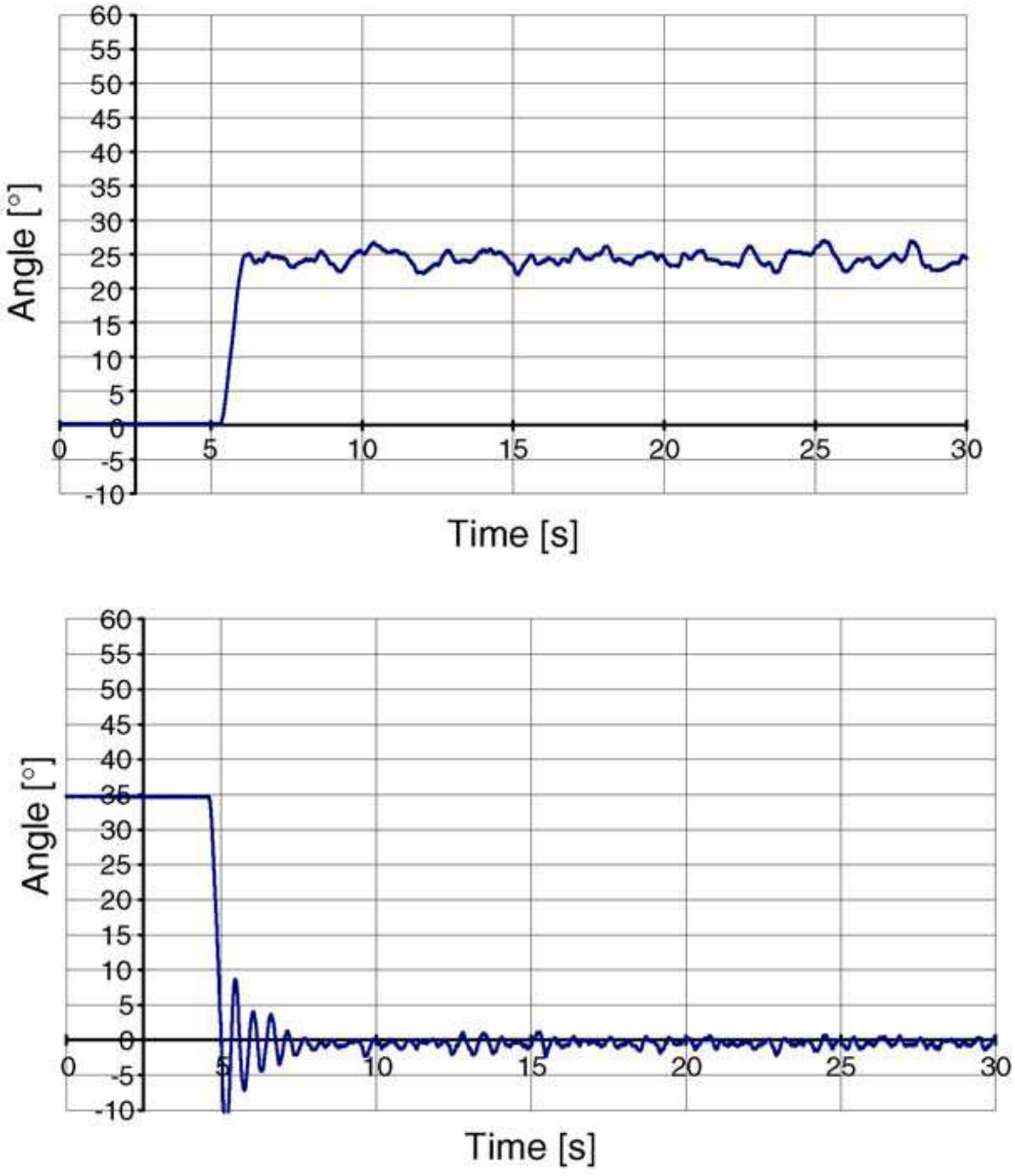


Figure 3: Time histories of roll angle for $\Lambda = 50°$ and $\alpha = 15°$ (top) and $\alpha = 35°$ (bottom).

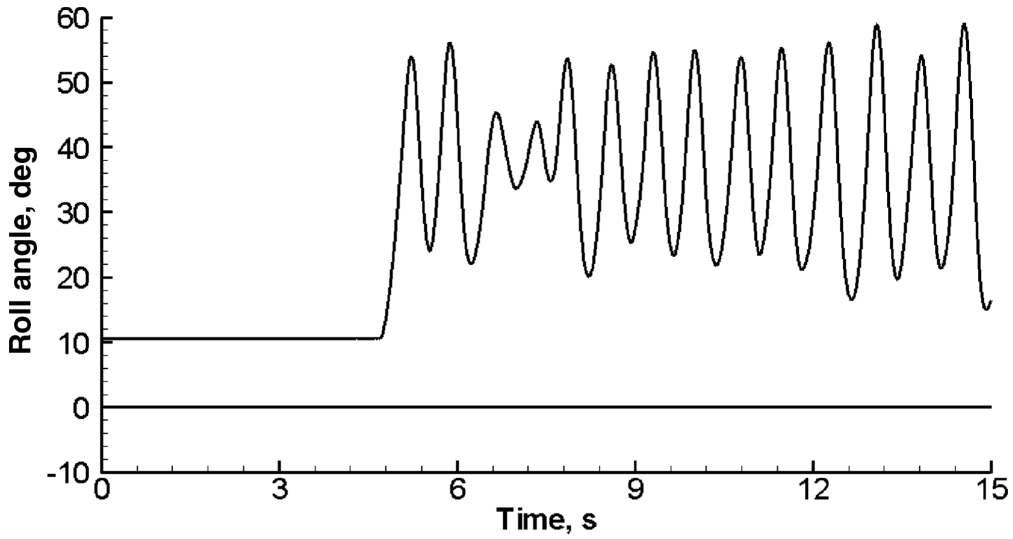


**a)**

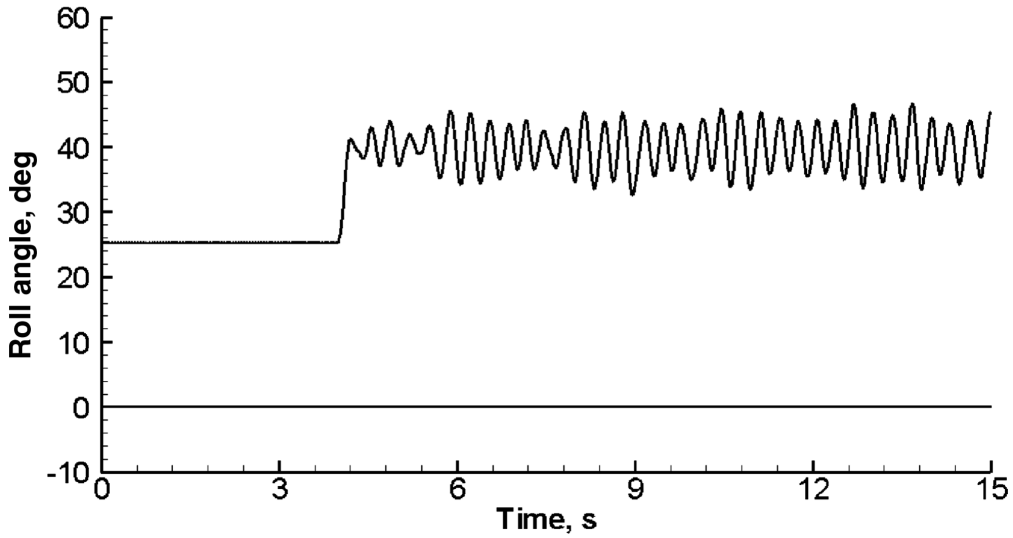


**b)**

Figure 4: Time history of roll angle for $\Lambda = 50°$ for a) thick wing with round leading-edges at $\alpha = 27.5°$, and b) thin wing with sharp leading edges at $\alpha = 22.5°$.

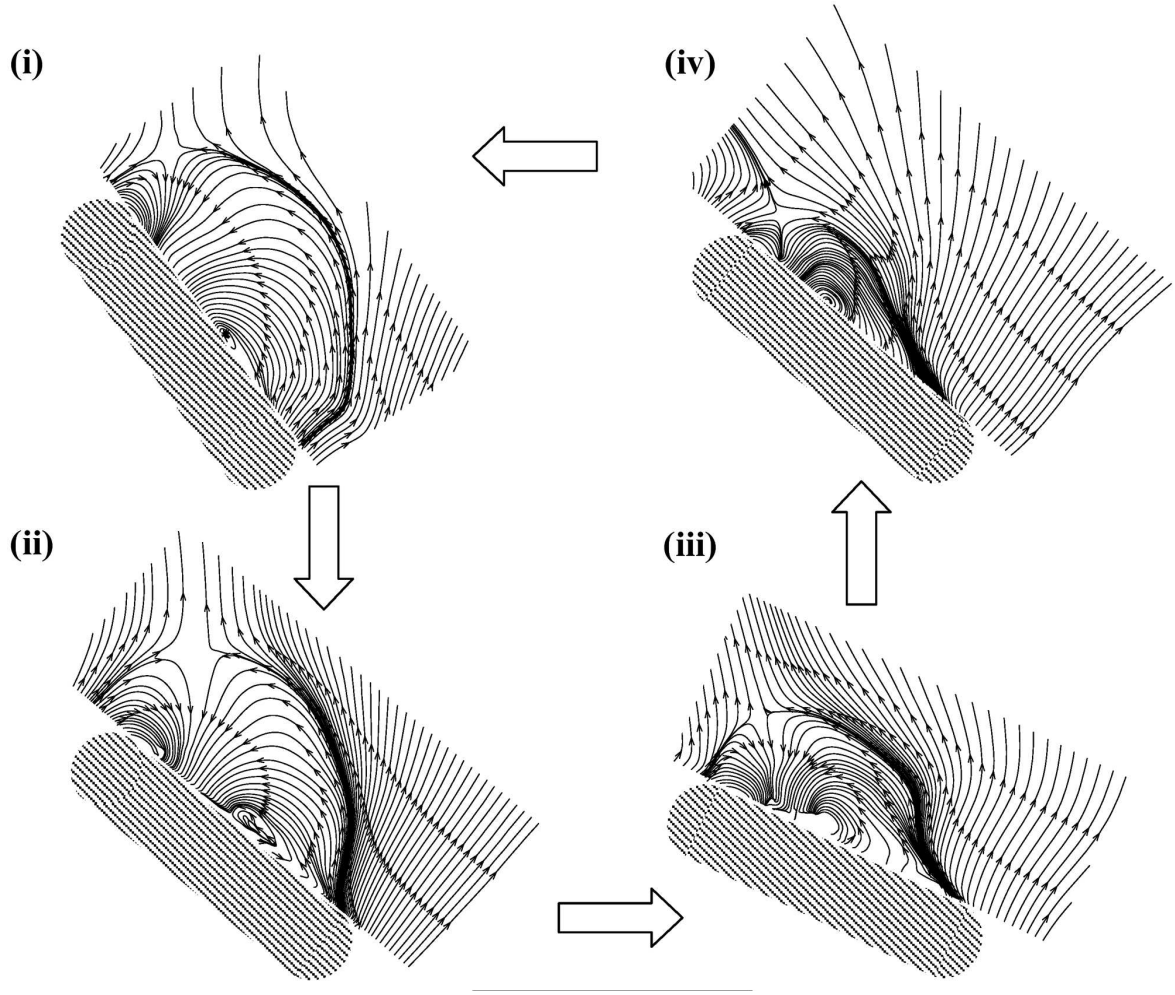


Figure 5: Crossflow streamlines at different phases of the roll oscillations, $\alpha = 28°$.

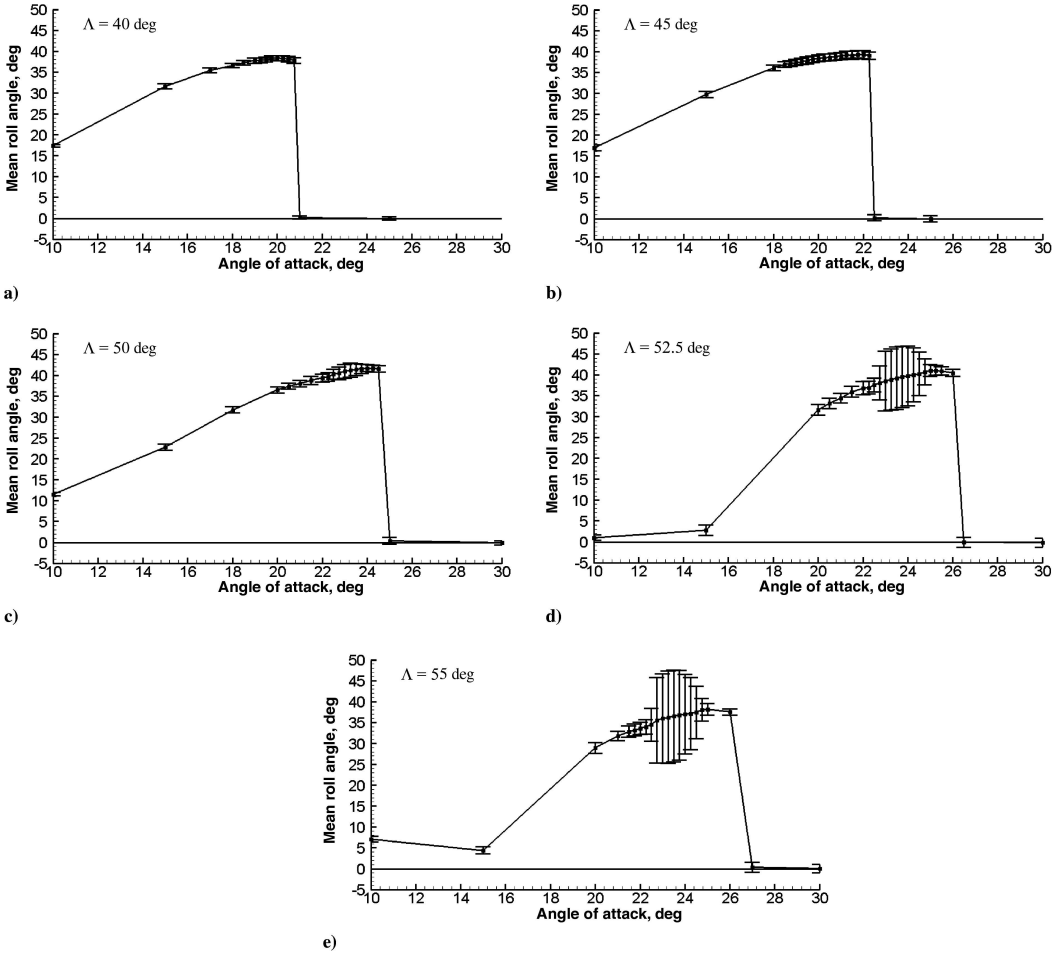


Figure 6: Variation of mean roll angle and standard deviation for slender wings.

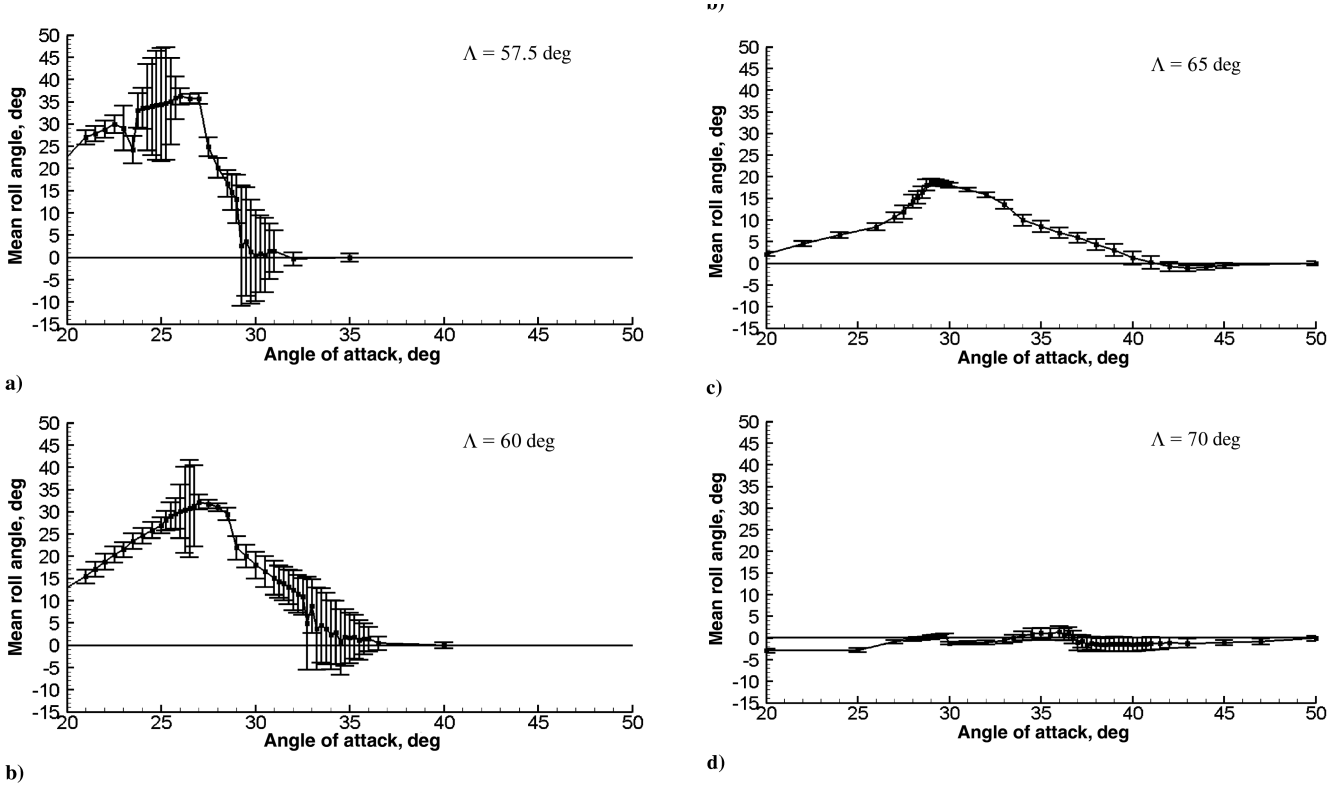


Figure 7: Variation of mean roll angle and standard deviation for nonslender wings.

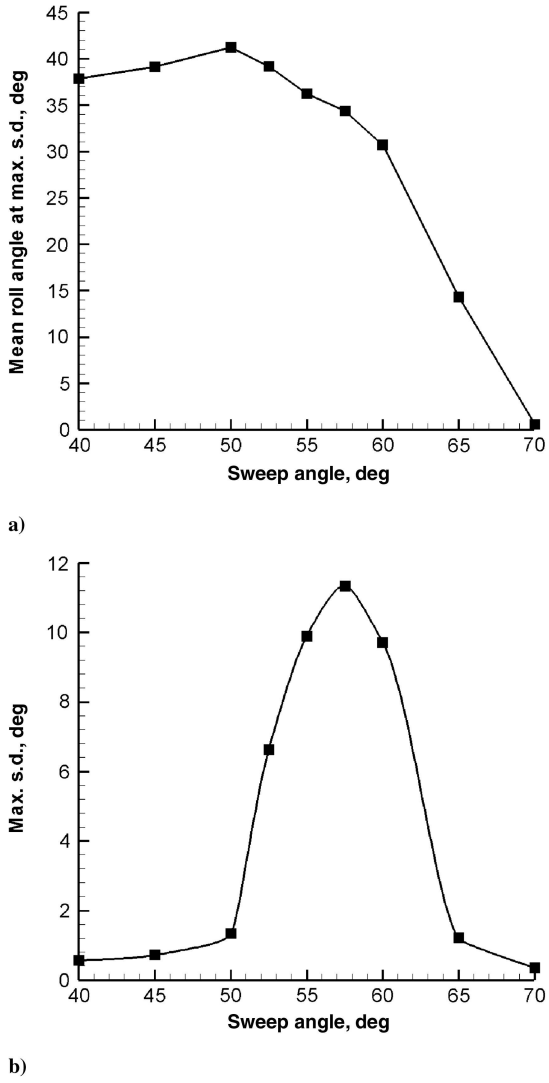


Figure 8: Variation of mean roll angle at angle of attack with highest standard deviation and maximum standard deviation as a function of sweep angle.

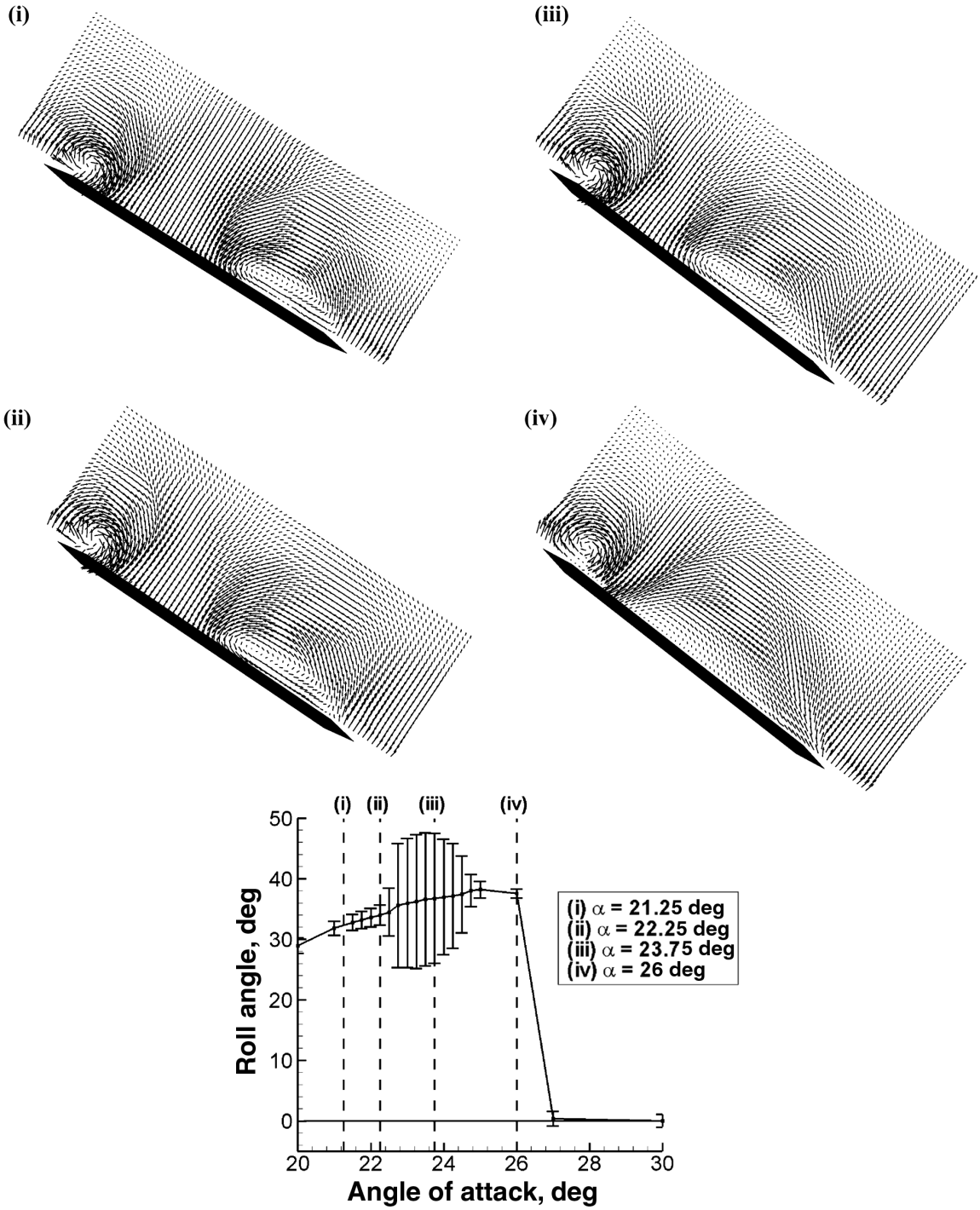


Figure 9: Crossflow velocity field for stationary wing and graph of mean roll angle with standard deviation as error bars as a function of incidence, $\Lambda = 55°$.

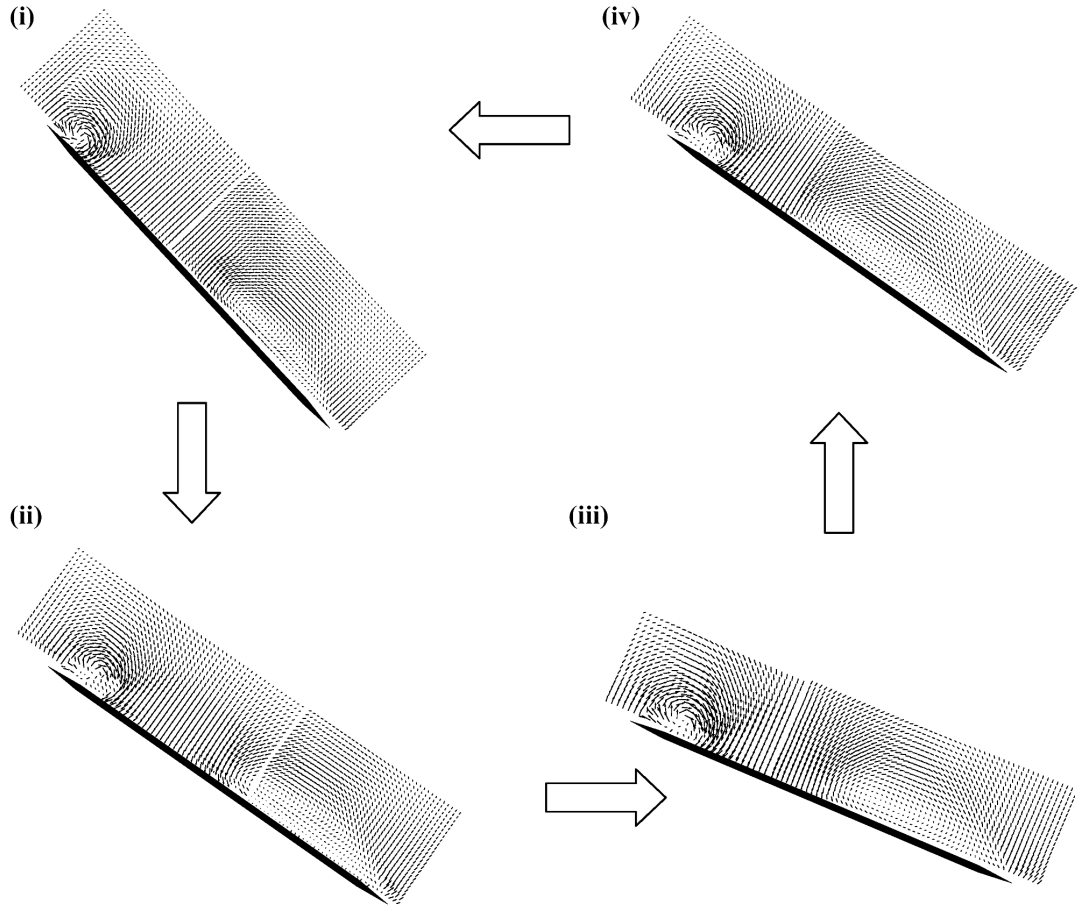


Figure 10: Phase-averaged crossflow velocity at different phases of the roll oscillations, $\alpha$ = 23.75° and $\Lambda$ = 55°.

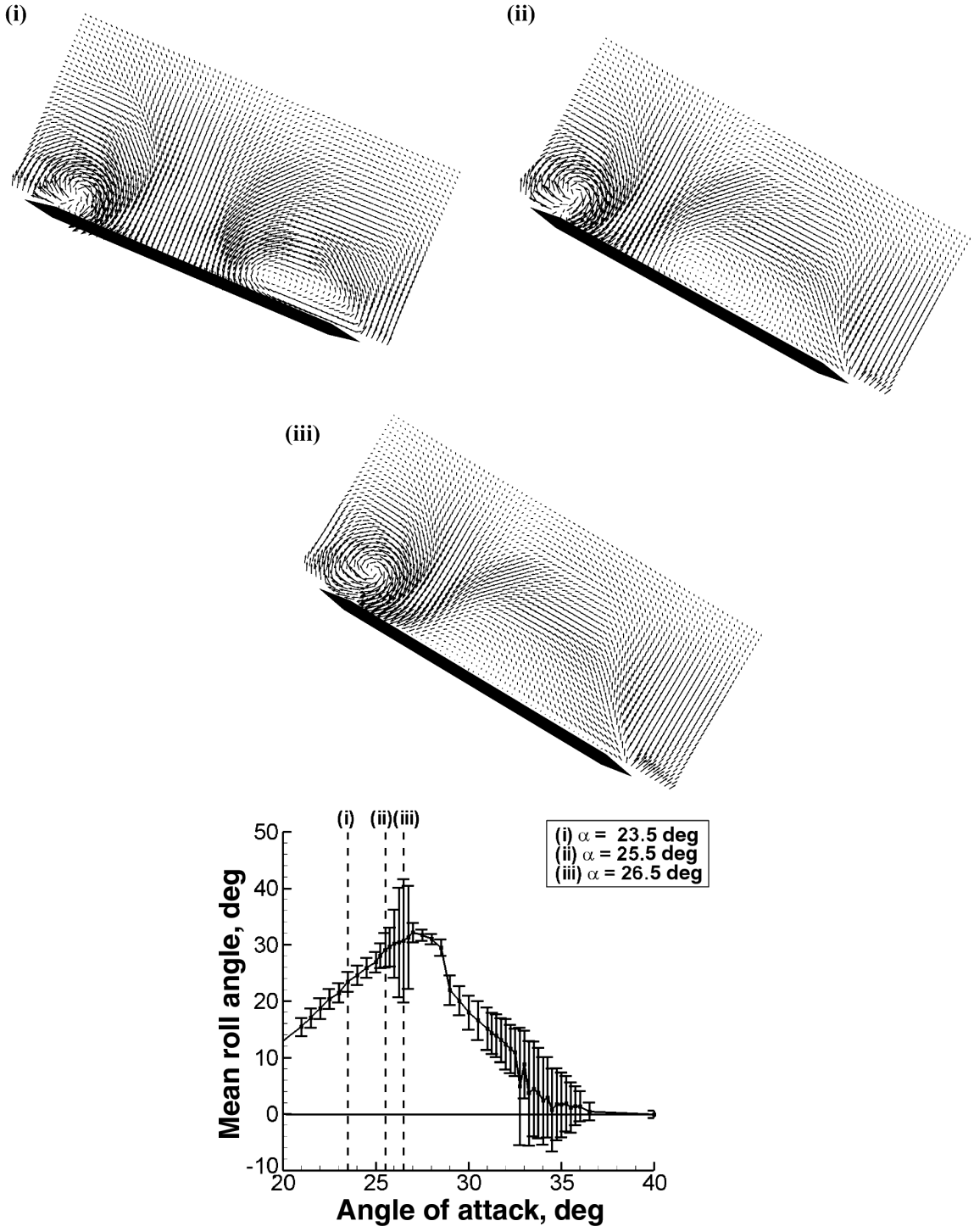


Figure 11: Crossflow velocity field for stationary wing and graph of mean roll angle with standard deviation as error bars as a function of incidence, $\Lambda = 60°$.

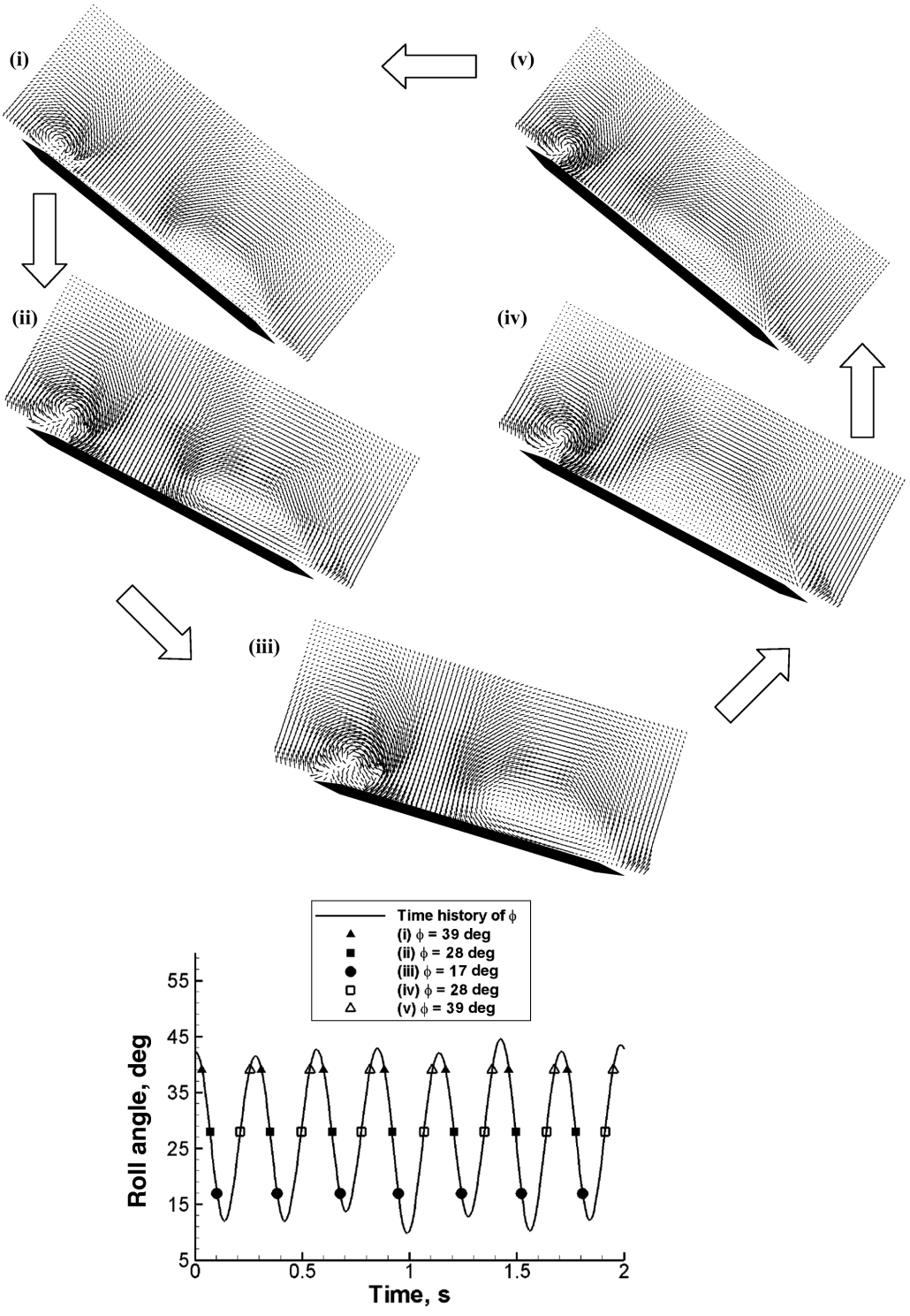


Figure 12: Phase-averaged crossflow velocity at different phases of the roll oscillations, and timing diagram corresponding to images for $\alpha = 26.5°$ and $\Lambda = 60°$.

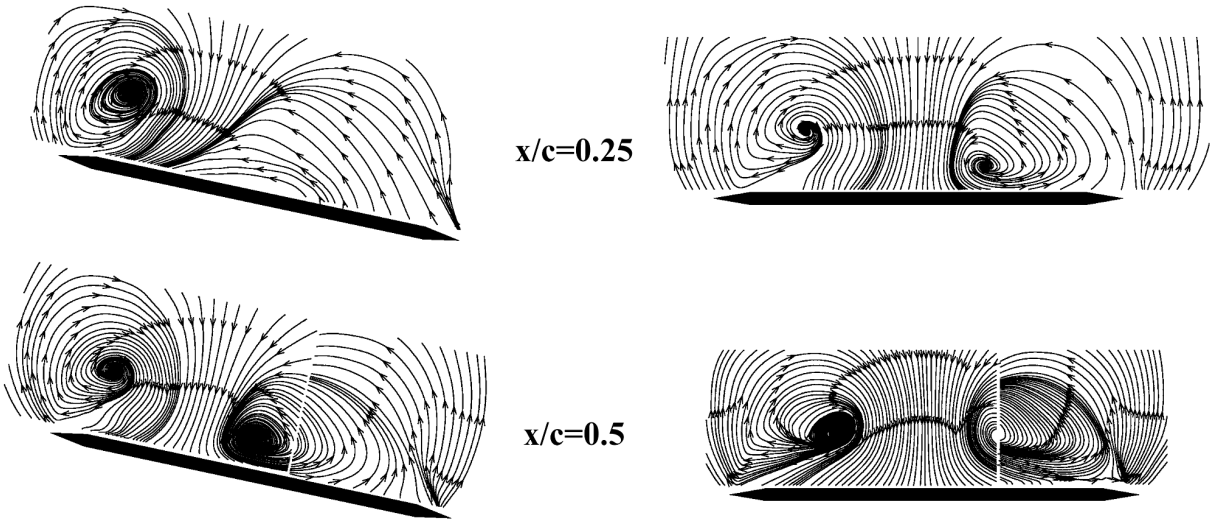


Figure 13: Crossflow streamline patterns near maximum and minimum roll angles, $\alpha = 33°$ and $\Lambda = 60°$.

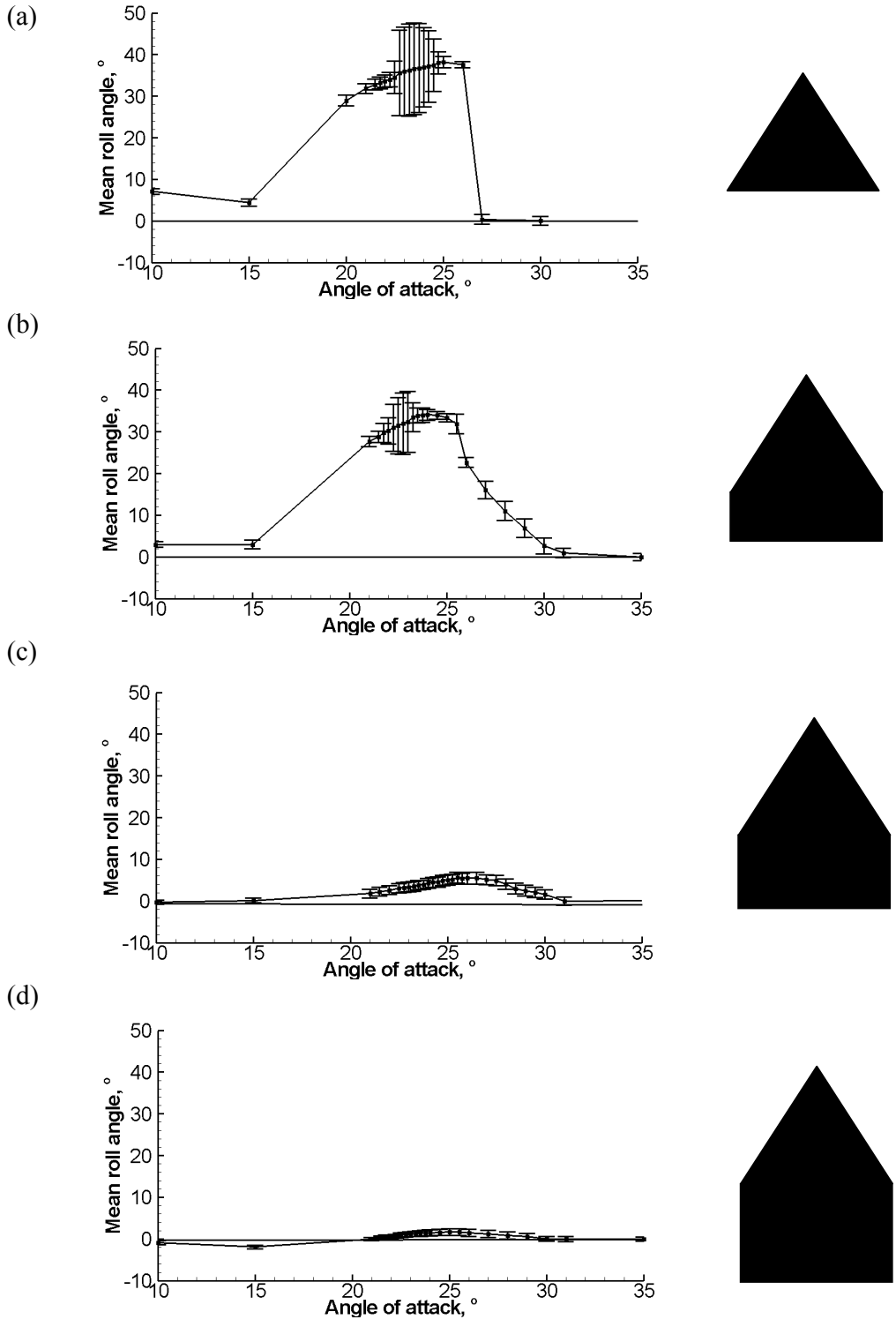


Figure 14: Graphs showing mean roll angle against angle of attack with standard deviation as error bars and schematics of each wing (right) for a) simple delta wing and b-d) cropped delta wings with different cropped section lengths, all with $\Lambda = 55^{o}$ and sharp leading-edges.

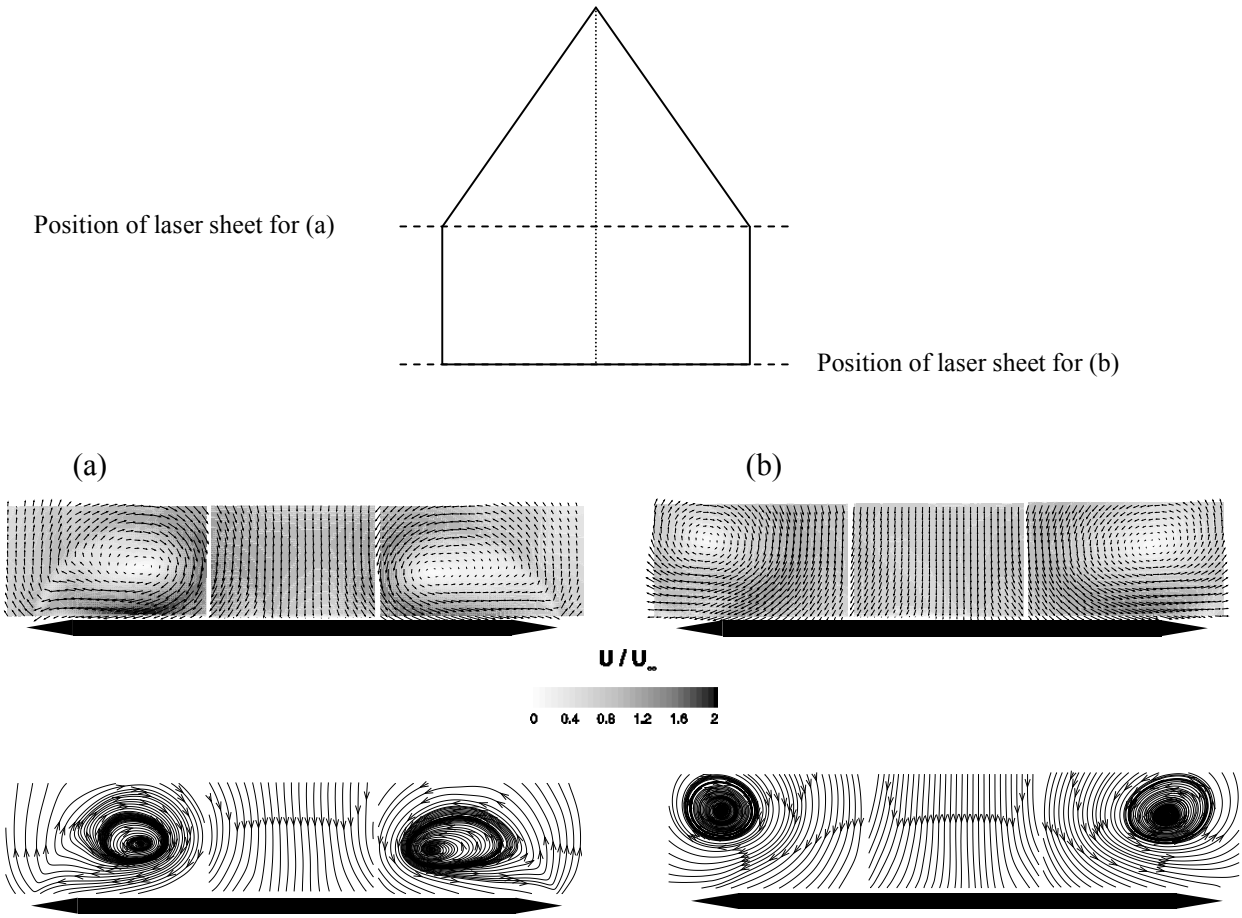


Figure 15: Cross-flow velocity and streamlines for stationary wing for (a) x/c = 39.5% and (b) trailing edge, at $\alpha = 20^o$ and $\Phi = 0^o$ for cropped delta wing with $\Lambda = 55^o$ and sharp leading-edge, together with schematic of laser sheet locations (top).

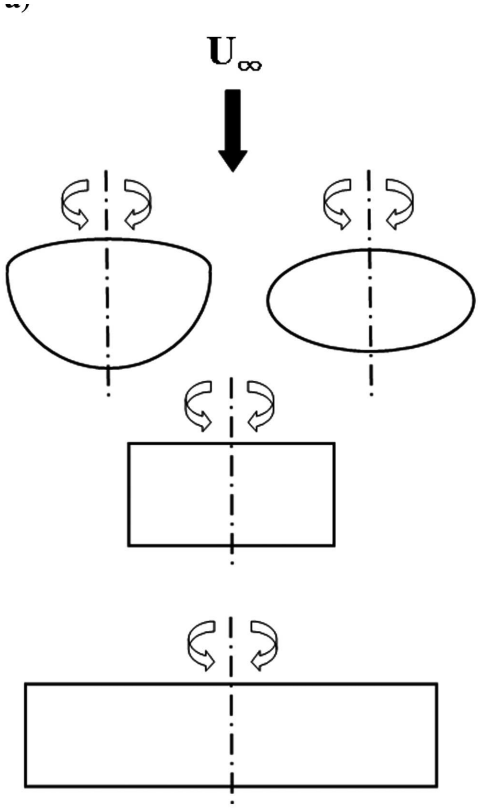


Figure 16: Planform shapes, with Zimmerman, elliptical, and rectangular wings.

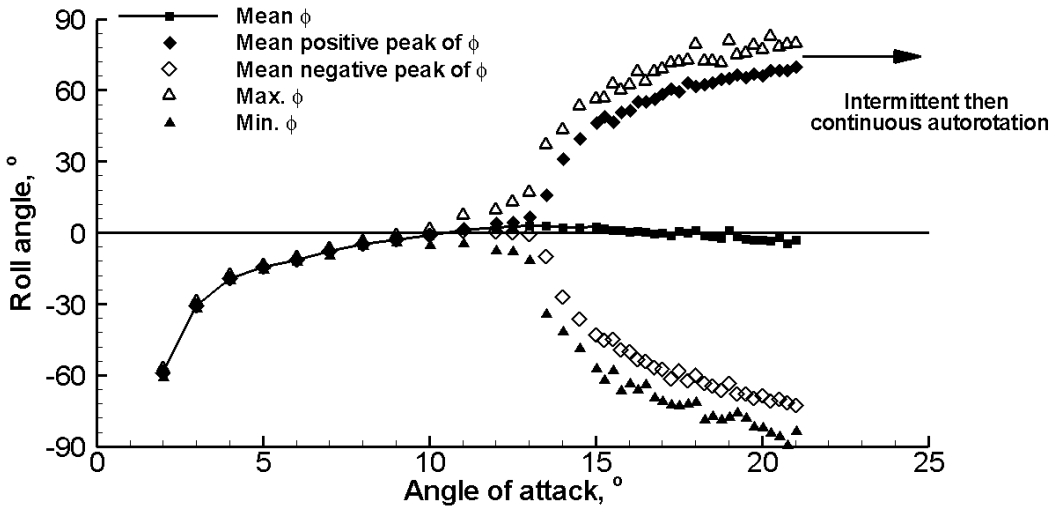


Figure 17: Variation of roll angle with angle of attack for the rectangular wing, AR = 2.

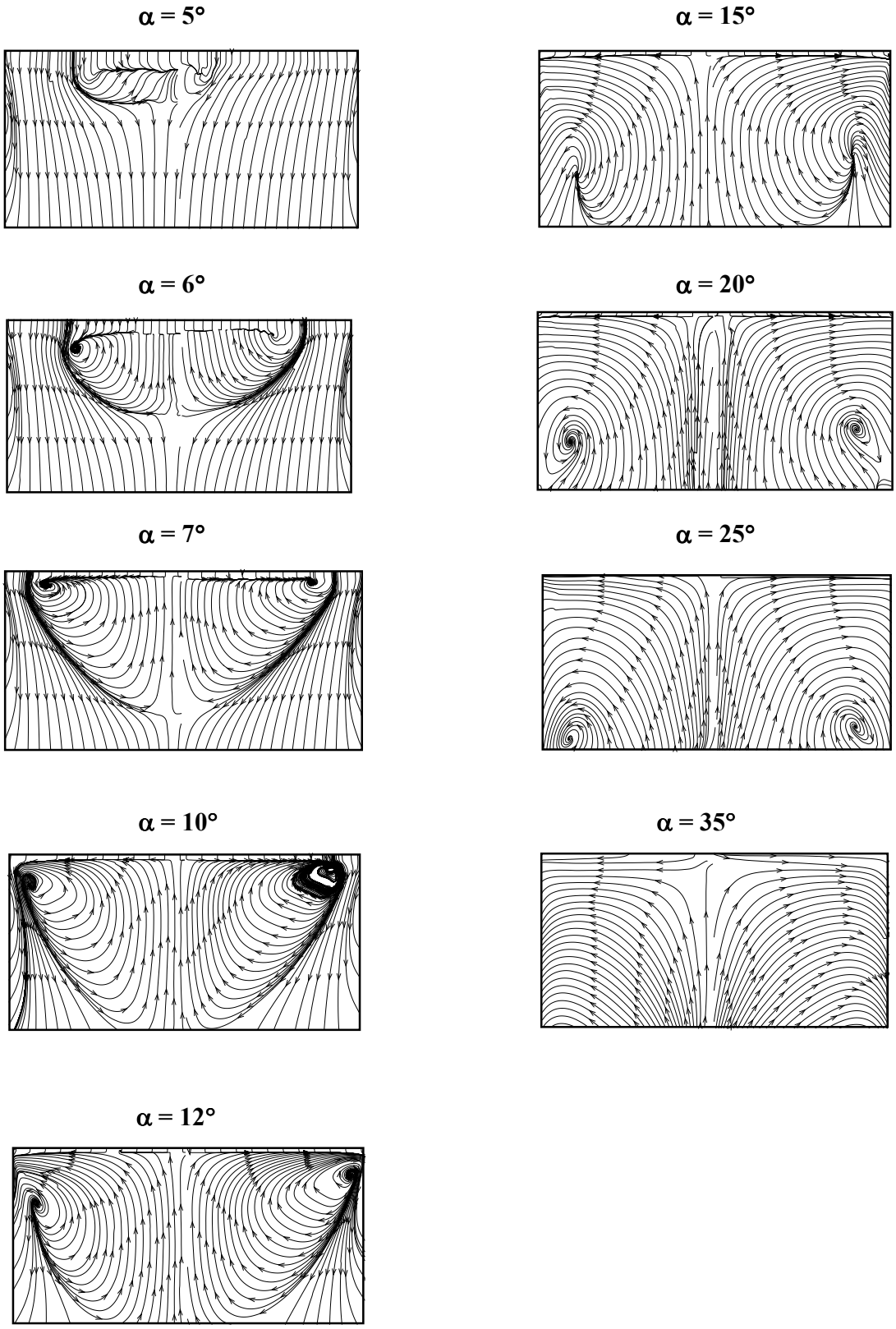


Figure 18: Near-surface streamlines for a stationary rectangular wing at zero roll angle for various angles of attack.

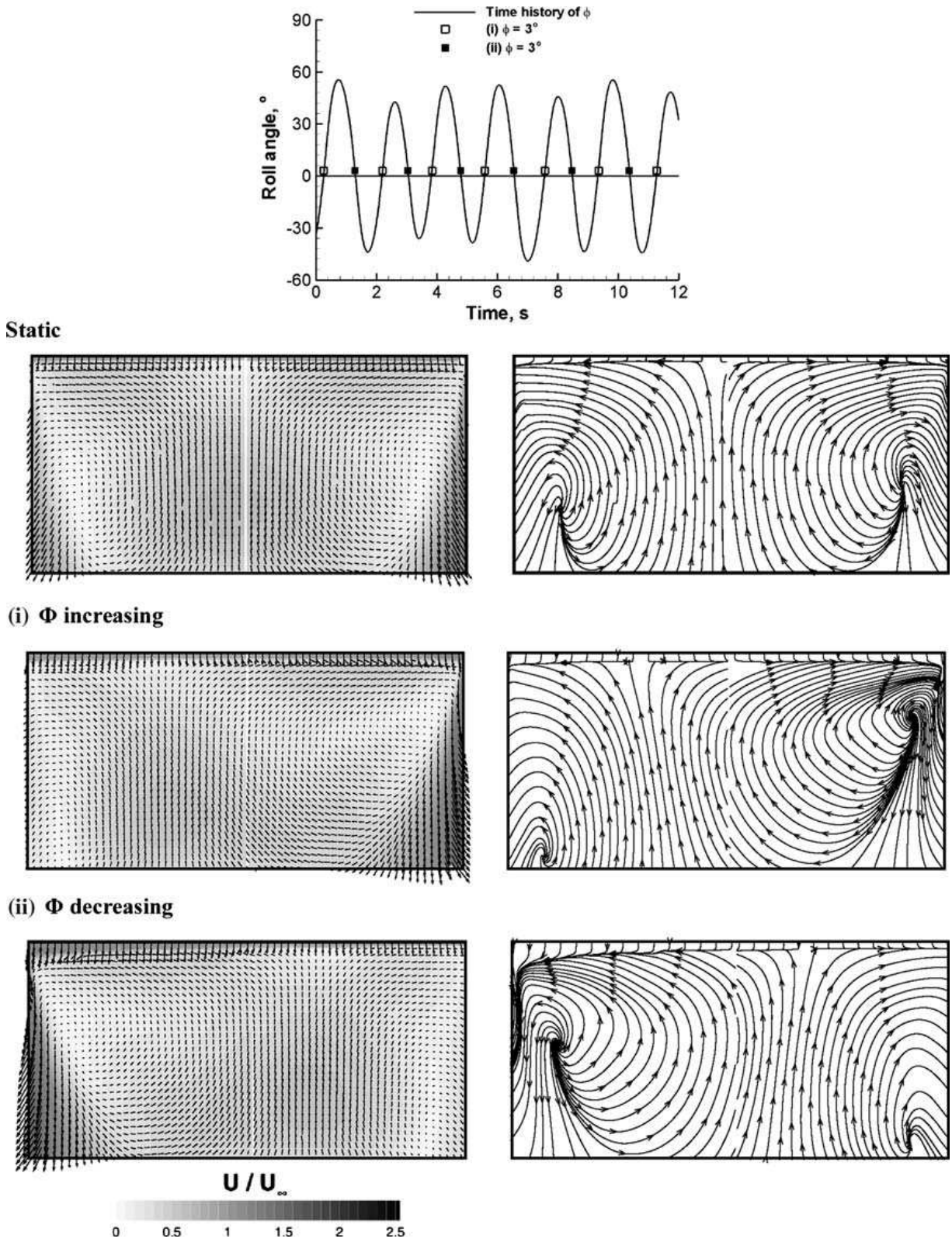


Figure 19: Near-surface velocity and streamline patterns at the mean roll angle for the static wing, for roll angle increasing and decreasing, $\alpha = 15°$.

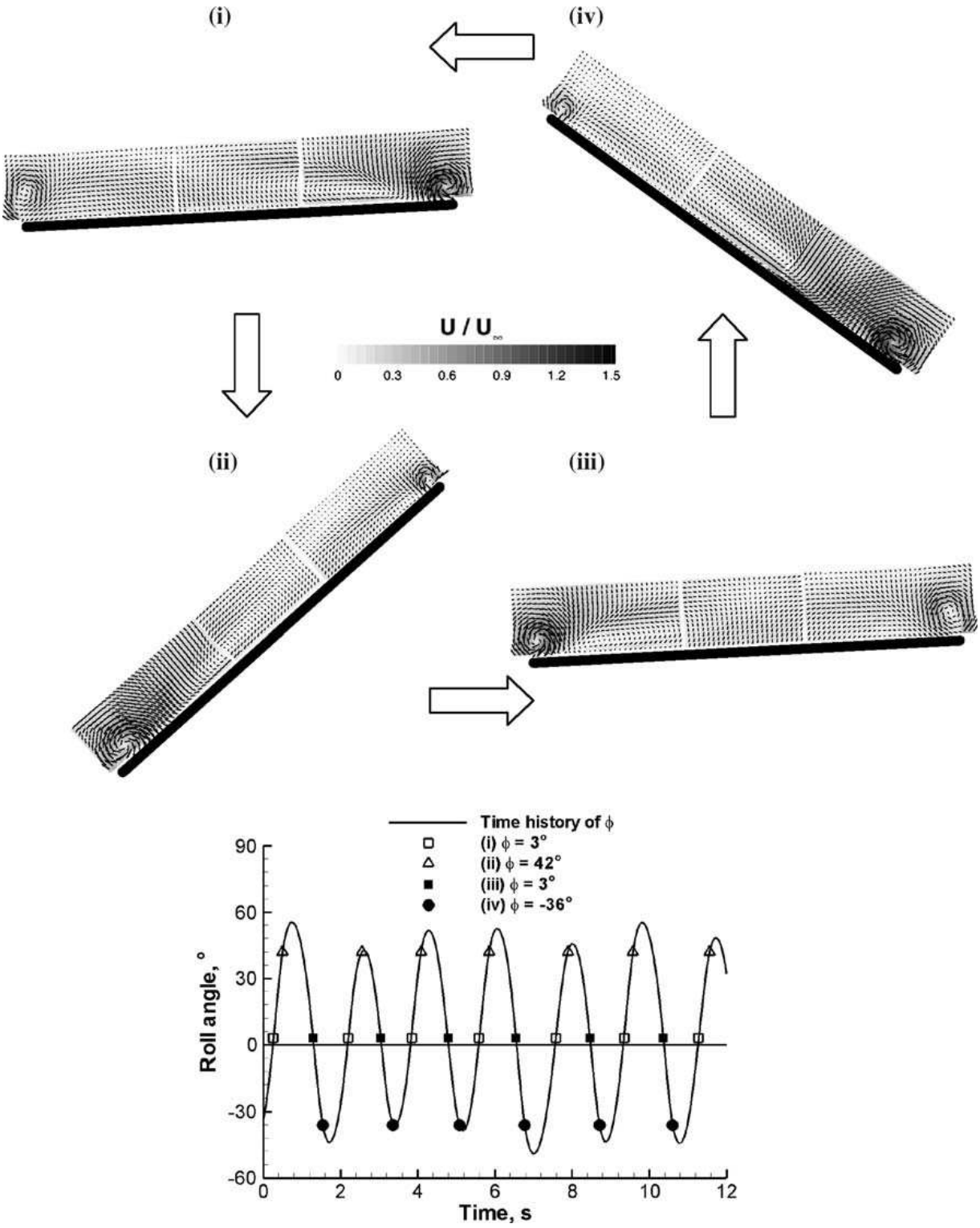


Figure 20: Crossflow velocity at different phases of the roll oscillations for rectangular wing, AR = 2, $\alpha = 15°$. The inset shows the roll angles at which measurements are taken.

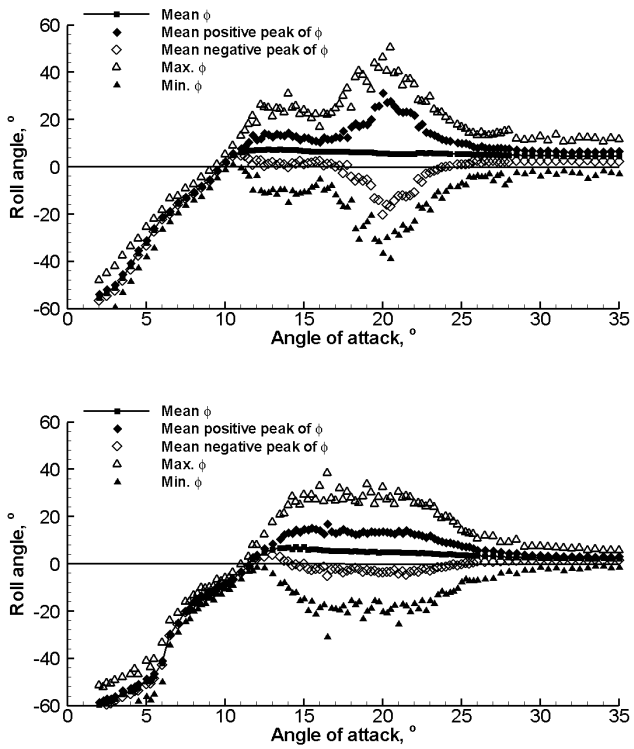


Figure 21: Graphs of roll angle for the elliptical wing (top) and Zimmerman wing (bottom).

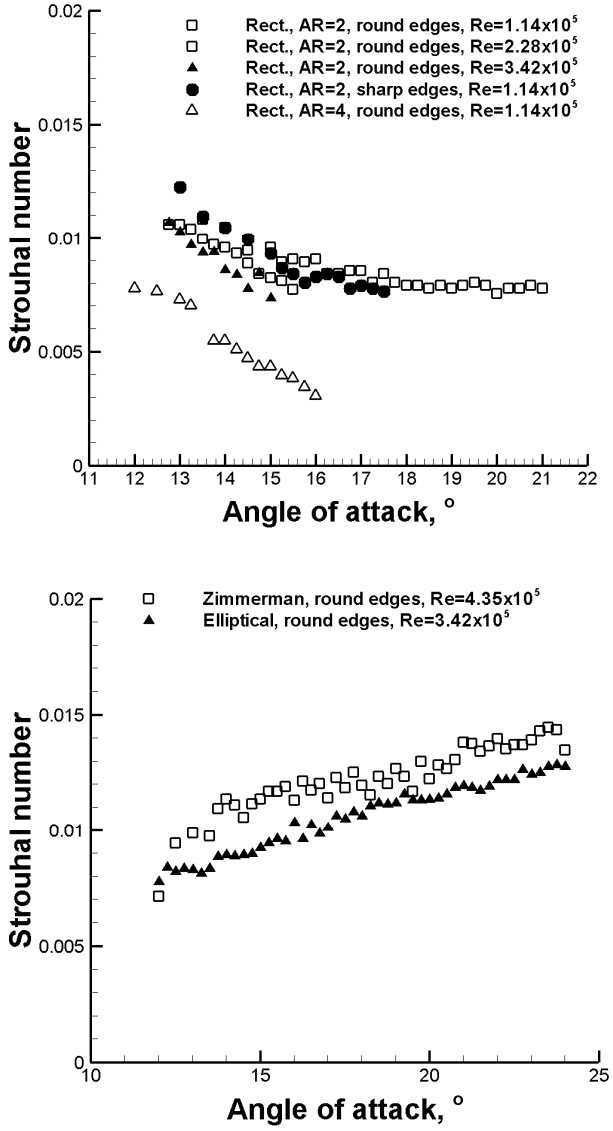


Figure 22: Strouhal number of the roll oscillations as a function of angle of attack for rectangular, Zimmerman and elliptical wings.